USING THE BULLET CLUSTER AS A GRAVITATIONAL TELESCOPE TO STUDY $Z \gtrsim 7$ LYMAN BREAK GALAXIES

Nicholas Hall[1], Maruša Bradač[1], Anthony H. Gonzalez[2], Tommaso Treu[3,x], Douglas Clowe[4,y], Christine Jones[5], Massimo Stiavelli[6], Dennis Zaritsky[7], Jean-Gabriel Cuby[8], and Benjamin Clément[8]

Draft version January 11, 2012

ABSTRACT

We use imaging obtained with the Hubble Space Telescope Wide Field Camera 3 to search for z_{850} dropouts at $z \sim 7$ and J_{110} dropouts at $z \sim 9$ lensed by the Bullet Cluster. In total we find 10 z_{850} dropouts in our 8.27 arcmin^2 field. Using magnification maps from a combined weak and strong lensing mass reconstruction of the Bullet Cluster and correcting for estimated completeness levels, we calculate the surface density and luminosity function of our z_{850} dropouts as a function of intrinsic (accounting for magnification) magnitude. We find results consistent with published blank field surveys, despite using much shallower data, and demonstrate the effectiveness of cluster surveys in the search for $z \sim 7$ galaxies.

Subject headings: gravitational lensing – galaxies: high redshift

1. INTRODUCTION

The properties of the first galaxies in the universe are of particular interest given their likely role in the reionization of the intergalactic medium (IGM). This phase change of the universe from highly neutral to highly ionized is believed to have begun several hundred million years after the Big Bang and ended $\lesssim 900$ million years after the Big Bang (corresponding to $z \gtrsim 6$) (see e.g., Fan et al. 2006; Larson et al. 2011). However, recent observations of $z \gtrsim 6$ star-forming galaxies are not yet conclusive as to whether the observed bright end of the population could alone be responsible for reionization, or whether we need to invoke faint objects in higher numbers or with larger stellar masses producing more rest-frame UV photons (e.g., Bouwens et al. 2008; Stark et al. 2009; Bouwens et al. 2011). To answer this question, more high redshift observations that probe the faint end of the population are essential. Observational constraints on the fraction of photons from these early galaxies that escape into the IGM, and the clumpiness of the neutral Hydrogen (HI) in the IGM are also needed.

Lyman break galaxies (LBGs) provide the largest and best-studied sample of high redshift galaxies (see e.g., Vanzella et al. 2009 for a recent study and Giavalisco

Electronic address: nrhall@ucdavis.edu
[1] Department of Physics, University of California, One Shields Avenue, Davis, CA 95616
[2] Department of Astronomy, University of Florida, 211 Bryant Space Science Center, Gainesville, FL 32611, USA
[3] Department of Physics, University of California, Santa Barbara, CA 93106, USA
[4] Department of Physics & Astronomy, Ohio University, Clippinger Labs 251B, Athens, OH 45701
[5] Harvard-Smithsonian Center for Astrophysics, 60 Garden Street, Cambridge, MA 02138, USA
[6] Space Telescope Science Institute, 3700 San Martin Drive, Baltimore, MD 21218, USA
[7] Steward Observatory, University of Arizona, 933 N Cherry Ave., Tucson, AZ 85721, USA
[8] Laboratoire d'Astrophysique de Marseille, OAMP, Université Aix-Marseille & CNRS, 38 rue Frédéric Joliot Curie, 13388 Marseille cedex 13, France
[x] Sloan Fellow, Packard Fellow
[y] Sloan Fellow

2002 for a review). Their spectra exhibit a sharp decrease in energy at wavelengths below the Lyman limit (the Lyman Break) due to more energetic photons being absorbed within the LBG itself. For LBGs at $z \gtrsim 6$, further absorption below Lyα (the Lyα Break) occurs in intervening HI clouds. Their high rest-frame UV luminosity blueward of Lyα and distinctive spectral break enable detection of these galaxies out to high redshift through the "dropout" technique. This technique utilizes the significant drop in galaxy flux as you move blueward of the break. LBGs have been detected at $z \sim 5$ as V-band dropouts, $z \sim 6$ as i-band dropouts, $z \sim 7$ as z-band dropouts, $z \sim 8$ as Y-band dropouts, and even $z \sim 9 - 10$ as J-band dropouts. (e.g., Giavalisco et al. 2004; Henry et al. 2008; Stark et al. 2009; Castellano et al. 2010a; Bouwens et al. 2011). Standard selection criteria have been developed for detecting dropouts in a desired redshift range and avoiding interlopers outside that range (e.g., Giavalisco et al. 2004; Beckwith et al. 2006; Bouwens et al. 2007, 2008). As an example of their effectiveness, Vanzella et al. (2009) using followup spectroscopic observations find that only 10% of their $z \sim 4$, 5 and 6 dropout-selected sources from the Great Observatories Origins Deep Survey (GOODS) are interlopers (83% of which are galactic stars).

Despite the effectiveness of the dropout technique, high redshift galaxy detection is greatly complicated not only by low apparent brightness due to high luminosity distances but also low intrinsic brightness due to low stellar masses compared to moderate redshift ($z \sim 2 - 3$) galaxies (e.g., Bouwens et al. 2007). This results in faint observed magnitudes for sources at $z \sim 7$. The ability to detect high redshift galaxies can be greatly enhanced by the use of galaxy clusters as gravitational telescopes, as proposed by Soucail (1990), in that these galaxies are magnified and thus have brighter observed magnitudes. This method has been implemented successfully by various authors to study galaxies over a wide range of redshifts (e.g., Altieri et al. 1999; Blain et al. 1999; Ellis et al. 2001; Metcalfe et al. 2003; Richard et al. 2006, 2008; Bouwens et al. 2009; Zheng et al. 2009; Bradley

et al. 2011) and is responsible for some of the highest redshift galaxies detected at the time of their discovery (e.g., Kneib et al. 2004; Bradley et al. 2008).

The light from distant galaxies can be magnified by several orders of magnitude as a result of the large gravitational potential well of an intervening massive galaxy cluster. This magnification provides increased depth at the cost of decreased observed solid angle. By way of number counts, the effective slope of the Luminosity Function (LF) being sufficiently steep ($\beta_{eff} = -d(\log\Phi)/d\log L > 2$) over the range of magnitudes probed results in a positive magnification bias in that reaching fainter magnitudes by means of lensing more than compensates for the fewer sources resulting from decreased observational solid angle (e.g., Broadhurst et al. 1995). Such steep effective slopes have been found at $z \sim 7$ all the way down to $L \sim 0.1L^*$ (or $M_{1600\text{\AA}} \simeq -17.8$, Bouwens et al. 2011)[11]. Going to even fainter magnitudes can still result in increased cumulative number counts as the loss at low luminosity is overcompensated by the steepness of the LF at the bright end. Thus the surface density of LBGs can increase significantly as a result of the magnification provided by cluster surveys yielding a much improved statistical analysis of the numerous fainter sources.

In addition to the number of galaxies detected, magnification has the positive consequence of increased spatial resolution, thus allowing better examination of high redshift galaxies on smaller physical scales. In blank field surveys of color-selected galaxies it is often impossible to confirm the nature of candidate high redshift galaxies given the similarity of their colors with cold Milky Way stars. Also, due to photometric scatter lower redshift ($z \sim 1-2$) elliptical galaxies and moderate redshift ($z \sim 2-3$) dust-reddened star-forming galaxies can enter the high redshift selection window. In cluster surveys however lensed galaxies can be elongated, if they are resolved, thus removing stars as contaminants. Clusters can also multiply-image background galaxies in a redshift-dependent way, thus removing lower redshift galaxy contaminants. For multiply-imaged systems, the positions of the images are redshift dependent. A $z > 5$ multiply-imaged source can therefore be readily distinguished from a multiply/singly imaged $z \sim 2$ source and foreground (single) stars, provided accurate lensing maps are available. Cluster surveys are therefore better capable than blank field surveys of differentiating high redshift galaxies from interlopers. In addition, the magnification provided by clusters can better facilitate spectroscopy of $z \gtrsim 7$ galaxies, like that of Vanzella et al. 2011 in which the first robust LBGs were confirmed at $z > 7$ (see also, Santos et al. 2004; Stark et al. 2007).

There are various ingredients that make a specific cluster a better suited cosmic telescope for the study of such high-z galaxies. A more massive cluster produces larger areas of intermediate to high ($\mu > 2$) magnification. A low redshift cosmic telescope would be desirable (as the angular area of high magnification is large), however this results in undesirable amounts of obscuration of background galaxies by cluster members. Hence clusters of intermediate ($\sim 0.3 - 0.5$) redshift are better suited for

these studies. Detailed cluster magnification maps are essential for the lensed galaxy analysis. These maps are best constrained in clusters with many strongly lensed images. In addition, lenses that are highly elliptical in the plane of the sky are desirable because they have larger areas of high magnification. As a result they also tend to have more arcs and are thus easier to model. Given these considerations, cluster 1E0657-56 (Bullet Cluster) is in many ways ideal. Discovered by Tucker et al. (1995), it is very hot and X-ray luminous, highly elongated, and at an optimal redshift for these studies ($z \sim 0.296$).

In this work we search for $z \gtrsim 7$ galaxies in new deep infrared (IR) data of the Bullet Cluster obtained with the Wide Field Camera 3 (WFC3, Kimble et al. 2008) aboard the Hubble Space Telescope (HST). Following Bradač et al. (2009), we optimally combine strong lensing data (including the positions of the multiply-imaged source discussed below) with ground and space-based weak-lensing data using adaptive grid to reconstruct the magnification map of the Bullet Cluster. With this map we estimate the intrinsic brightness of the LBGs that we detect as dropouts as well as the actual observed solid angle of our observations.

This paper is organized as follows. We describe the observations and data products in Section 2. In Section 3 we discuss our magnification maps of the Bullet Cluster. In Section 4 we discuss our photometry. In Section 5 we outline the selection criteria employed to search for $z \gtrsim 7$ galaxies, consider various possible sources of contamination, and present our final dropout sample. We estimate the completeness of our search in Section 6. In Section 7 we consider the surface density and luminosity function of our dropout sample. We summarize main results in Section 8. Where necessary, we assume cosmological parameters consistent with 7-year *Wilkinson Microwave Anisotropy Probe* (WMAP) data: $\Omega_m = 0.26$, $\Omega_\lambda = 0.74$, $h = 0.71$, and $\sigma_8 = 0.8$. All the coordinates in this paper are given for the epoch J2000.0. All magnitudes are given in the AB system (Oke & Gunn 1983).

2. OBSERVATIONS AND DATA REDUCTION

We obtained HST/WFC3 imaging on 19-20 November 2009 (Cycle 16, proposal 11099, PI Bradač), and with the Advanced Camera for Surveys (ACS, Ford et al. 2003) on 12-13 October 2006 (Cycle 15, proposal 10863, PI Gonzalez) and 12 October 2004 (Cycle 13, proposal 10200, PI Jones). The new WFC3 data consist of two WFC3/IR pointings in F110W (hereafter J_{110}, 6530s per pointing) and F160W (hereafter H_{160}, 7030s). The two pointings have an overlapping region centered on the cluster in which the above quoted exposure times are doubled, which are the numbers quoted in Gonzalez et al. (2010). The ACS/WFC imaging used here consists of two pointings centered on the main cluster. The main cluster has been imaged in F606W (hereafter V_{606}, 2340s), F775W (hereafter i_{775}, 10150s), and F850LP (hereafter z_{850}, 12700s), while the subcluster has been imaged in F435W(2420s), F606W (2340s), and F814W (7280s). For the high-redshift galaxy survey described below, we primarily use the main cluster's V_{606}, i_{775}, z_{850}, J_{110}, and H_{160} data as described below.

We use the Multidrizzle (Koekemoer et al. 2002) routine to align and combine the images. To register the

---

[11] For the LF parameterized following Schechter 1976, where $\beta_{eff} = -\alpha + L/L^*$)

images we determine the offsets among the images by extracting high S/N objects in the individual, distortion corrected exposures. We use SExtractor (Bertin & Arnouts 1996) and the IRAF routine geomap to identify the objects and calculate the residual shifts and rotations of individual exposures, which were then fed back into Multidrizzle. We use square as the final drizzling kernel and an output pixel scale of $0.1''$, smaller than the original pixel scale of the WFC3/IR CCD allowing us to exploit the dithering of the observations and improve the sampling of the point-spread function (PSF). Limiting magnitudes were estimated using $0.63'' \times 0.63''$ square apertures, which is approximately the same area on average that SExtractor attributed to each object (obtained from the segmentation file) in our final z_{850} dropout catalog. The 5σ limiting magnitudes for V_{606}, i_{775}, z_{850}, J_{110}, and H_{160} are 27.0, 26.4, 26.0, 26.4, and 26.1, respectively.

We also utilize data from the Infrared Array Camera (IRAC, Fazio et al. 2004) onboard NASAs Spitzer Space Telescope (*Spitzer*) to assist in the discrimination of contaminants in our high redshift LBG search. These data were obtained on 2004 December 17-18 and include imaging in all four IRAC bands ([3.6 μm], [4.5 μm], [5.8 μm], and [8 μm]) with effective exposure times of 4 ks in each filter (see Gonzalez et al. 2009 for details).

3. MAGNIFICATION MAPS OF THE BULLET CLUSTER

An accurate mass distribution of the Bullet Cluster is needed to obtain a magnification map from which the intrinsic (true, accounting for magnification) magnitudes of our high redshift dropouts can be determined given their lensed (observed) magnitudes. This mass distribution is reconstructed from the optimal use of multiply-imaged systems (strong lensing) and distortions of singly imaged background sources (weak lensing). The reconstruction is described in detail in Bradač et al. (2009) (for some other examples of reconstruction techniques using strong and weak lensing see Natarajan & Kneib 1996; Kneib et al. 2003; Smith et al. 2005; Diego et al. 2007; Jee et al. 2007; Limousin et al. 2007; Merten et al. 2009). The reconstruction does not assume a specific form of the underlying gravitational potential. It is performed on a pixelized adaptive grid, with more pixels nearer to the cluster and multiple images where the S/N of lensing is higher. Specifically, the course grid (in the outskirts where only weak-lensing data is available) is set to be $18''$/pixel. The grid is refined by a factor of 4 in the inner circular region ($1.5'$ radius around the Brightest Cluster Galaxy), and by a factor of 16 in the regions where we see multiple images. This gives a final resolution of $\sim 1''$/pixel. For the reconstruction we use the ACS and WFC3 images described above as well as the data used in Bradač et al. (2006) and Clowe et al. (2006). We obtain a new model closely following the methodology of Bradač et al. (2009). In this model we use the catalog of strongly lensed images from Bradač et al. (2009), with the addition of the spectroscopically measured redshift of multiply-imaged system K (z=2.79; Gonzalez et al. 2010). We also experiment with including the potential multiply-imaged system discussed in Section 5.4. Including this system results in a change in our intrinsic counts that is well within the error bars. The weak-lensing catalogs are taken from Clowe et al. (2006) and are obtained from a combination of ACS and ground-based data that

extend to a large FOV; we use the inner $9' \times 9'$ here.

Small-scale substructure not accounted for in the lens model (due to a finite number of multiply-imaged systems and erroneous redshifts) will result in uncertainties in the magnification maps of our field. These magnification uncertainties will produce errors in our intrinsic (in absence of lensing) magnitudes and solid angle. Magnification error (σ_μ) maps from Bradač et al. (2009) conservatively model the effects of this substructure as follows. The main cluster and sub clusters were modeled as pseudoisothermal elliptical mass densities and the cluster galaxies were modeled as 30 Singular Isothermal Spheres (SISs). 50 mass clumps containing 8% of the total mass, which changes critical curve positions by $5 - 10''$ (more than the uncertainty with which multiple images are recovered), were also randomly distributed throughout the mass map. 100 realizations of this cluster substructure were generated. The errors on the magnification were calculated as the standard deviation of the mean magnification at each pixel. While we produce a new $z = 7$ magnification map, which includes the candidate multiple image of this work, we do not produce a new σ_μ map. Instead we use the map from Bradač et al. (2009) for a source at $z = 6$. This will be practically indistinguishable from the σ_μ map of a source at $z \sim 7$ due to the fact that the lensing strength (or angular diameter distance ratio between lens and source, and observer and source) at these redshifts for a lens at $z \sim 0.3$ is nearly constant (see e.g., Bartelmann & Schneider 2001).

Given that our σ_μ map used a previous mass reconstruction we cannot use the σ_μ values at the position of the dropouts. We also cannot use the average σ_μ at the magnification of the dropout, because the actual σ_μ may differ significantly from the average depending on position in the image plane. We therefore estimate σ_μ at the position of each dropout by using the σ_μ from the map at the pixel nearest the dropout where the mean magnification (from the 100 substructure realizations above) is within 10% of the magnification of the dropout. For our dropout sample the average distance from the dropout to this pixel is $10''$. These are the magnification errors that appear in Table 1 and that are also included in the error on the intrinsic magnitudes by adding them in quadrature with the photometric errors.

Errors in the magnitudes (lensed and intrinsic) will give rise to errors in the number of dropouts in each magnitude bin of the surface density and LF of our dropout sample. As an example, there may be a magnitude bin that contains no counts but does contain a significant fraction of the error bars of the dropouts that fall in neighboring bins. We correct our surface density and luminosity function for this by using the sum of the fractions of the 1σ error bars as the number of objects in each bin.

4. PHOTOMETRY

Galaxies were detected in the HST/WFC3 imaging data described in Section 2. We followed a procedure very similar to that of Stark et al. (2009) and Coe et al. (2006). We use SExtractor (Bertin & Arnouts 1996) in dual image mode with detection performed for our z_{850} dropout search in a combined $J_{110} + H_{160}$ image, thus improving the signal to noise and the measurement of the centroid, and for our J_{110} dropout search in an

H_{160} image. Photometry was performed in each of the V_{606}, i_{775}, z_{850}, J_{110}, H_{160} filters. All magnitudes were first corrected for foreground galactic extinction given the B-V color excess in the direction of the bullet cluster (Schlegel et al. 1998), and the corresponding extinction values from Sirianni et al. (2005)[12] for V_{606}, i_{775}, and z_{850} and from Schlegel et al. (1998) for J_{110} and H_{160}. This yields foreground galactic extinction values of (0.23, 0.16, 0.12, 0.07, 0.05) for (V_{606}, i_{775}, z_{850}, J_{110}, H_{160}), respectively. Aperture magnitudes were measured in fixed circular apertures of $0.8''$ diameter with SExtractor's MAG_APER and were used to measure colors. We correct the aperture magnitudes for varying PSF size as described below. The final magnitudes in each filter were computed using a combination of aperture colors and the SExtractor parameter MAG_AUTO of the reddest filter (H_{160}), i.e.,

$$m_x = \text{MAG\_AUTO}\,(H_{160}) + (\text{MAG\_APER}\,(H_{160}) - \text{MAG\_APER}\,(x)), \quad (1)$$

where x is V_{606}, i_{775}, z_{850}, and J_{110}.

There are various factors that need to be considered in our photometric analysis. First, intracluster light (ICL) occupies $\sim 20 - 25\%$ of our search area in J_{110} and H_{160} where it is brightest, as can be seen in the combined color image of Figure 1. Difficulties in determining the background given the presence of the ICL and in distinguishing between ICL and galaxy flux may introduce additional errors and/or a bias in our measured magnitudes. We carefully examine the uncertainties introduced by ICL as described below. Second, the inability of MAG_AUTO to pick up the wings of the PSF can lead to measured magnitudes that are too faint. Finally, the varying size of the PSF for the different wavelengths probed by the filters must be accounted for in the aperture magnitudes. We investigate our photometric errors and possible biases with detailed simulations in each band as follows.

We first choose objects from the stellar locus and estimate the full-width-half-max (FWHM) of the PSF, which we measure to be (0.16, 0.17, 0.17, 0.18, 0.19) arcsec in V_{606}, i_{775}, z_{850}, J_{110}, and H_{160}, respectively. This is slightly larger than the estimates of Bouwens et al. (2011) for example. This is expected given that we have fewer images and thus a larger multidrizzle dropsize (1.0), which is essentially the size of the top hat with which the PSF is convolved. We place 26th magnitude[13] stars in the image convolved with a PSF generated with Tiny Tim (Hook et al. 2008) with the above measured FHWM. Regarding the number of stars, we place a sufficient number uniformly in the image so that, given our completeness levels of Section 6, we detect ~ 100 of them and measure their magnitudes. We do this 5 times, combine these ~ 500 objects, and measure the mean and standard deviation of the distribution of measured magnitude minus input magnitude. We perform 3 sigma clipping from the median of the distribution to better measure the mean of the magnitude difference by excluding outliers, such as mock objects confused with

---

[12] Assuming an 05 V type star since these early star-forming galaxies should be dominated by young massive stars
[13] Chosen given that the average H_{160} magnitude of our z_{850} dropouts is 25.9

real objects in the image. For MAG_AUTO in H_{160} we measure a mean of 0.15 and standard deviation of 0.16. For comparison, using a Gaussian PSF we find a mean of -0.02 and standard deviation of 0.18, demonstrating the effect of an extended PSF. We also do this for the aperture magnitudes used for our colors. With the Tiny Tim PSF we find a mean of (0.04, 0.06, 0.04, 0.19, 0.18) and standard deviation of (0.11, 0.11, 0.14, 0.09, 0.12) in V_{606}, i_{775}, z_{850}, J_{110}, and H_{160}, respectively. Using a Gaussian PSF we find a mean of (0.00, -0.01, -0.01, -0.01, -0.01) and standard deviation of (0.10, 0.11, 0.13, 0.08, 0.12) in V_{606}, i_{775}, z_{850}, J_{110}, and H_{160}, respectively. As expected, the bias is smaller at shorter wavelengths for the Tiny Tim PSF due to the smaller PSF size resulting in a larger fraction of the object flux within the $0.8''$ diameter aperture. The difference between the ACS and WFC3 PSFs is also manifested.

For both MAG_AUTO in H_{160} and the aperture magnitudes in all of the bands, we correct for the biases found with the Tiny Tim PSF, which is currently our best estimate of the PSF shape. Even though the bias depends strongly on the PSF shape, a misestimate of 0.1-0.2 magnitudes would not significantly effect our our surface density and luminosity function given the large bin sizes used (see Sec. 7). We also use the standard deviations found with the Tiny Tim PSF, which does not depend significantly on the PSF shape, as the minimum photometric error on the magnitudes.

5. DROPOUT SELECTION

In this section we discuss our selection of z_{850} and J_{110} dropouts through the use of color and S/N criteria (Section 5.1), intrinsic brightness cuts (Section 5.2), and infrared (*Spitzer* and HAWK-I) data (Section 5.3). We then provide the properties of our final dropout sample as well as potentially interesting contaminants (Section 5.4). Finally we address the possibility of contamination from point sources.

5.1. *Color and S/N Criteria*

We select our z_{850} dropouts by requiring all of the following selection criteria:

$$z_{850} - J_{110} > 1.0 + 0.4(J_{110} - H_{160}) \quad (2)$$

$$z_{850} - J_{110} > 1.0 \quad (3)$$

$$J_{110} - H_{160} \leq 1.1 \quad (4)$$

$$S/N\,(H_{160}) > 3.5, \ S/N\,(J_{110}) > 3.5 \quad (5)$$

$$S/N\,(i_{775}) < 3, \ S/N\,(V_{606}) < 3. \quad (6)$$

We will refer to Equations 2, 3, and 4 as the "color criteria" and Equations 5 and 6 as the "S/N criteria". The color criteria are adapted from those of Bouwens et al. (2008), which were developed for HST/NIC3 J_{110} and H_{160}. To adjust them to be consistent with our filters we shift them by the amount by which the colors differ for a $z = 7$ template star-forming galaxy spectrum when measured with our filters versus those of Bouwens et al. (2008) (a difference of ~ 0.2 magnitudes). The template spectrum we use is from the isochrone synthesis code of Bruzual & Charlot (2003) with an instantaneous burst, an age of 100 Myr, metallicity of $Z = 0.008Z_\odot$, and no dust (See e.g., Labbé et al. 2010; Castellano et al. 2010b).
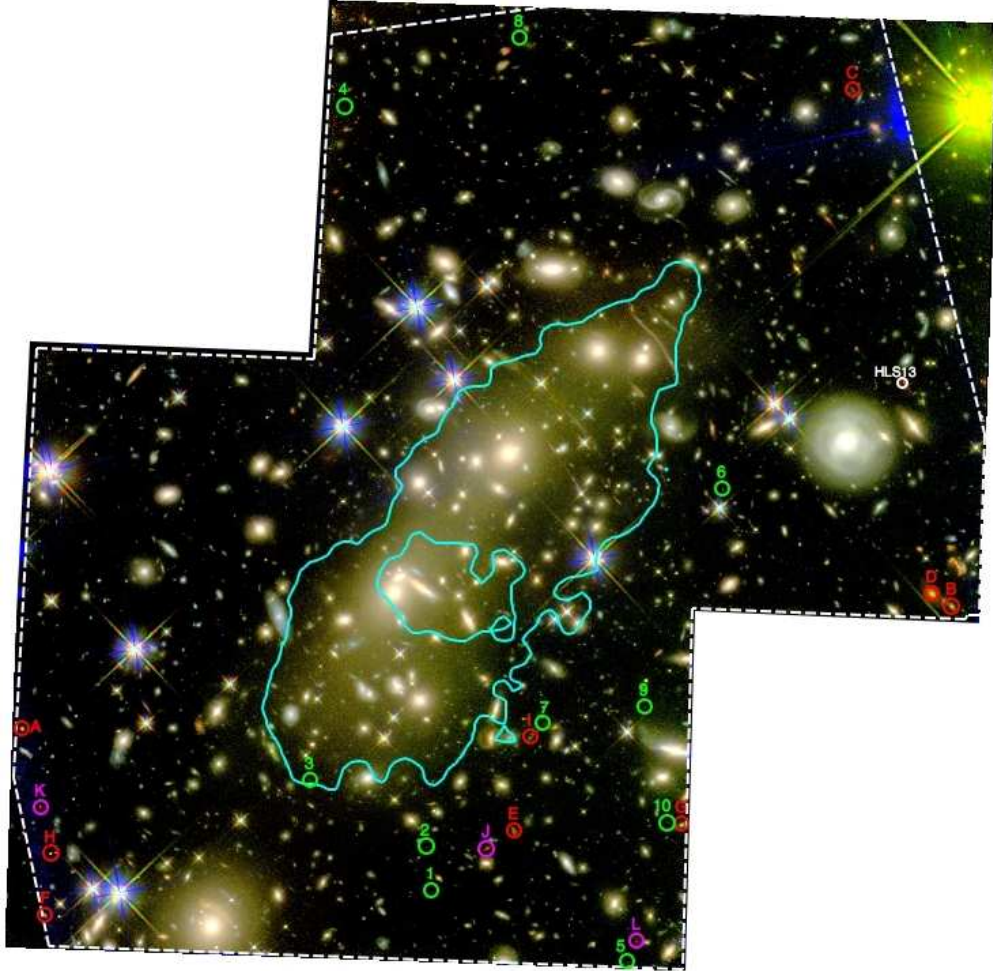
Figure 1. A combined color image of the Bullet Cluster (z_{850} = blue image, J_{110} = green image, and H_{160} = red image) with the search area outlined (*dashed white line*, showing the tilt of the z_{850} pointing relative to the two WFC3 pointings) and the curve of maximum magnification of the lens model overlaid (*cyan line*). The z_{850} dropout candidates are shown as *green circles* labelled with the numbers of Table 1. The z_{850} (J_{110}) dropout contaminants are shown as *red* (*magenta*) *circles* labelled with the letters of Table 2. The *Herschel* source HLS13 of Rex et al. (2010) is shown as a *white circle*. The image is $3.3' \times 3.3'$. North is up and East is left.

We refer to this template spectrum below as our "BC03 starburst template".

The S/N cut of Equation 5 corresponds to the requirement S/N($J_{110} + H_{160}$) $\gtrsim 5\sigma$. Deep blank field surveys typically impose S/N cuts of 2σ for the filters blue-ward of the dropout filter. However, given that we have less exposures to combine, we are likely to have more artifacts due to cosmic rays that can cause artificial detections. We thus impose 3σ S/N[14] cuts and then carefully inspect each object by eye in the V_{606} and i_{775} images and throw it out if it is detected. We also remove artifacts such as diffraction spikes and fake objects near the detector edges.

The above z_{850} dropout selection criteria select galaxies in the redshift range $6 \lesssim z \lesssim 9$ with a mean redshift of 7.5 for objects with $m_{H_{160}} = 26$ (see Figure 5 of Section 6). The selection window is shown as the grey shaded region in the z_{850}-J_{110} versus J_{110}-H_{160} color Figure 2. Sources that do not satisfy our dropout selection criteria are shown as green dots. The colors of low-mass

M, L, and T dwarf stars are expected to lie in the region enclosed by orange lines. The typical colors of various galaxy types are shown as they evolve in redshift (for our BC03 starburst template, a dusty galaxy from Chary & Elbaz 2001, and an elliptical, spiral, and irregular galaxy from Coleman et al. 1980).

We also search for J_{110} dropouts by requiring all of the following color and S/N selection criteria:

$$J_{110} - H_{160} > 1.1 \qquad (7)$$

$$S/N\,(H_{160}) > 5 \qquad (8)$$

$$S/N\,(z_{850}, i_{775}, V_{606}) < 3. \qquad (9)$$

Again, we also carefully inspect each object in the images and throw it out if it is detected in V_{606}, i_{775}, or z_{850}. The above J_{110} dropout selection criteria select galaxies in the redshift range $8 \lesssim z \lesssim 11$ with a mean redshift of 9.5 for objects with $m_{H_{160}} = 26$ (see Figure 5 of Section 6).

5.2. *Intrinsic Brightness Cuts*

The $4000\mathring{A}$ break of a $z \sim 1.4$ (2.0) elliptical galaxy will be at the same wavelength as the Lyman Break for

---

[14] Estimated as the flux divided by the flux error using the photometry discussed in Section 4.
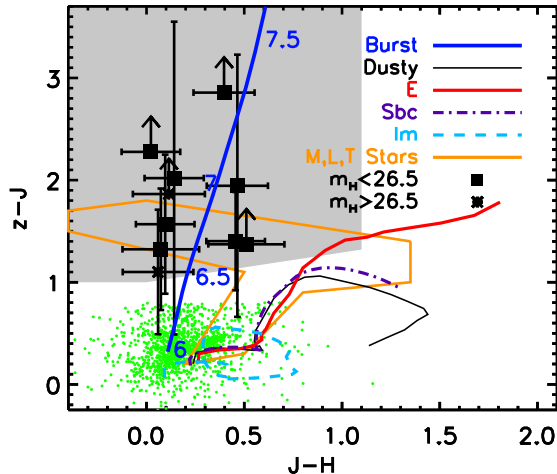
Figure 2. z_{850}-J_{110} versus J_{110}-H_{160} color-color diagram showing our z_{850} dropout selection window (*grey shaded region*). The colors of our z_{850} dropouts with $m_{H_{160}} < 26.5$, those used in the surface density and luminosity function, are shown (*black squares*) as well as those with $m_{H_{160}} > 26.5$ (*black asterisks*). Sources which do not satisfy our dropout selection criteria are shown in green. The redshift evolution of the colors of a Bruzual & Charlot (2003) star-forming galaxy with low metallicity ($Z = 0.008Z_{\odot}$), an age of 100 Myr, no dust, and attenuated for IGM absorption as a function of redshift according to Madau (1995) is shown with a *blue line*. The colors of a Chary & Elbaz (2001) dusty galaxy (Dusty,*thin black line*) and a Coleman et al. (1980) elliptical (E, *red line*), spiral (Sbc, *dot-dashed purple line*), and irregular galaxy (Im, *dashed cyan line*) are also shown as they evolve in redshift. The *orange lines* show region in which we expect T Dwarf colors to lie (Knapp et al. 2004).

a $z \sim 7$ (9) LBG. These elliptical galaxies as well as dust-reddened galaxies may enter the red portion of our selection window through photometric scatter.

These lower redshift galaxies are on average intrinsically brighter than the high z LBGs we are targeting. We thus exclude bright interlopers by rejecting those objects intrinsically brighter than the brightest LBG we might expect to see. We estimate the brightest intrinsic H_{160} apparent magnitude we might see as follows. A $10L^*$ galaxy[15] at $z = 6$ (7.5), the lowest redshift allowed by our z_{850} (J_{110}) selection criteria, would have an apparent magnitude of 24.0 (24.2). We reject 2 z_{850} dropout candidates and 1 J_{110} dropout candidate that have intrinsic H_{160} apparent magnitudes $m_{H_{160,int}}$ (obtained from the observed $m_{H_{160}}$ and the magnification at the position of the object from the $z = 7$ magnification map) brighter than this cut.

5.3. *Infrared Data*

Whereas bright lower redshift elliptical and dusty galaxies can be rejected with S/N and intrinsic magnitude cuts, fainter objects are not as easily excluded. Contamination from faint elliptical and dusty galaxies in our z_{850} dropout catalog is expected to be minimal given

[15] We use the Bouwens et al. (2011) best fit $z \sim 7$ (8) LF to determine the L^* used for z_{850} (J_{110}) dropout intrinsic brightness cut.

that our candidates do not have colors consistent with them (to at least one sigma, see Figure 2). We nevertheless utilize our longer wavelength data to aid in distinguishing these contaminants from high redshift LBGs. For our z_{850} dropouts we consider the H_{160} - [3.6μm] (*Spitzer* Chanel 1) color of these galaxies. Whereas our BC03 starburst template at $z = 7$ has H_{160} - [3.6μm] = 1, many ellipticals and dusty galaxies are significantly redder than this. For example, both the elliptical and dusty galaxy templates used in Figure 2 begin to have H_{160} - [3.6μm] > 1 at $z = 1.3$. By $z = 3$ the elliptical (dusty) template has H_{160} - [3.6μm] = 2.8 (2.1). The H_{160} - [3.6μm] color for dusty galaxies can vary widely depending on how dusty the galaxy is and its redshift. As an extreme example, we consider the dusty lensed galaxy behind the bullet cluster, which has $A_V \sim 3.8$ (Gonzalez et al. 2010). We can detect a galaxy such as this one, with H_{160} - [3.6μm] = 3.75, at 3σ in [3.6μm] for sources as faint as $m_{H_{160}} = 26$. Whereas, some of these fainter ellipticals and dusty galaxies will be detected in [3.6μm], we do not expect our z_{850} dropouts to be, which is in fact the case for all of the objects in our sample.

There are two objects that satisfy our J_{110} color criteria, S/N criteria, and intrinsic brightness cut, referred to below as objects J and L in Table 2 and Figure 4 (object K does not satisfy the intrinsic brightness cut). They are both quite bright; object J (L) has $m_{H_{160,int}} = 24.8 \pm 0.2$ (24.6 ± 0.2) and is thus only 0.6 ± 0.2 (0.4 ± 0.2) magnitudes fainter than the intrinsic brightness cut. Both objects are clearly detected in [4.5μm] in our *Spitzer* data. In [3.6μm] object J is clearly detected but object L can't unambiguously be separated from another nearby brighter galaxy. We do not expect our high redshift LBGs to be detected in [3.6μm] (as discussed above) or in [4.5μm]. In addition, both of these objects are detected in the Ks-band of the High Acuity, Wide field K-band Imaging (HAWK-I, Kissler-Patig et al. 2008) camera on the Very Large Telescope (VLT) and have H_{160} - Ks ~ 0.5. Our BC03 starburst template would have to be at $z \sim 11$ in order to have an H-K color 0.5. It is very unlikely that these objects are at such high redshift given their intrinsic brightnesses. On the other hand, a dusty galaxy spectrum from Chary & Elbaz (2001) at $z = 1.9$ (2.3) fits the J_{110}, H_{160}, and Ks-band data of object J (L) quite well. These facts lead us to believe that these objects are most likely low redshift interlopers and thus we do not consider them high redshift candidates, and do not include them in the rest of our analysis.

5.4. *Final Dropout Sample*

Upon implementing the above z_{850} dropout selection criteria, we obtain a final sample of 10 z_{850} dropouts, with cutout images shown in Figure 3 and properties given in Table 1. The z_{850} dropouts are also shown as green circles in Figure 1. Only those z_{850} dropouts with $m_{H_{160}} < 26.5$, where the completeness is greater than 22% (See Section 6) are used in the surface density and luminosity function below. These 8 objects are shown as the black squares in Figure 2, whereas the 2 objects with $m_{H_{160}} > 26.0$, are shown as asterisks. Upon implementing all the J_{110} dropout selection criteria, we find no J_{110} dropout candidates.

The majority of the z_{850} dropouts (7 out of 10) are found in the bottom right portion of Figure 1. This is

Dropout	R.A.	Decl.	m$_{H_{160}} \pm \Delta_{\rm p}$	$(J_{110} - H_{160})$	$(z_{850} - J_{110})$	μ	m$_{H_{160},\rm int} \pm \Delta_{\rm l+p}$
1	104.65470	-55.974464	26.77±0.23	0.11±0.18	>1.3	4.3±0.2	$28.34^{+0.24}_{-0.24}$
2	104.65527	-55.971901	26.97±0.23	0.06±0.18	1.10±0.61	6.5±0.5	$28.99^{+0.25}_{-0.25}$
3	104.66736	-55.968067	24.97±0.16	0.46±0.15	1.40±0.48	12±4	$27.67^{+0.35}_{-0.47}$
4	104.66375	-55.928802	26.37±0.22	0.51±0.19	>1.3	2.8±0.08	$27.46^{+0.22}_{-0.22}$
5	104.63437	-55.978603	25.91±0.22	0.07±0.20	1.32±0.59	2.1±0.03	$26.71^{+0.22}_{-0.22}$
6	104.62446	-55.951065	25.85±0.19	0.02±0.15	>2.1	10.±2	$28.37^{+0.28}_{-0.31}$
7	104.64304	-55.964756	25.81±0.26	0.14±0.15	2.02±1.53	5.2±0.5	$27.61^{+0.28}_{-0.28}$
8	104.64549	-55.924828	25.89±0.21	0.40±0.16	>1.9	3.1±0.1	$27.12^{+0.22}_{-0.22}$
9	104.63254	-55.963764	26.00±0.16	0.46±0.16	1.94±1.28	4.3±0.3	$27.59^{+0.17}_{-0.18}$
10	104.63015	-55.970482	26.37±0.16	0.10±0.15	1.57±0.68	3.0±0.2	$27.57^{+0.17}_{-0.17}$

Note. — The final error on m$_{H_{160},\rm int}$ ($\Delta_{\rm l+p}$) includes errors in the lensing (magnification) and photometry added in quadrature. z$_{850}$-J$_{110}$ lower limits are the 1σ limiting magnitudes computed in the vicinity of the dropout.
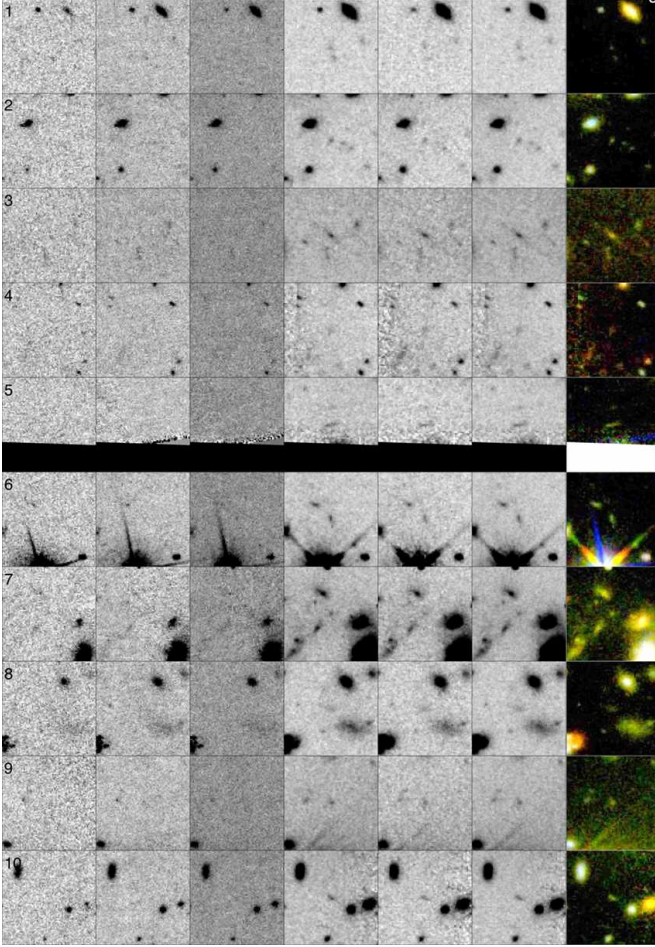

Figure 3. Cutouts of our z$_{850}$ dropouts shown (from left to right) in V$_{606}$, i$_{775}$, z$_{850}$, J$_{110}$, H$_{160}$, J$_{110}$ + H$_{160}$, and a z$_{850}$J$_{110}$H$_{160}$ color image. The numeric labels correspond to the labels of Table 1. The cutouts are 7″ × 7″. To get an idea of physical size, for a source at $z = 7$ (9) and in the absence of lensing, 7″ corresponds to 37 (32) kpc. For a uniform magnification of 12, the highest in our z$_{850}$ dropout sample, 7″ corresponds to an intrinsic length of 11 (9.1) kpc for a source at $z = 7$ (9).

likely due to a combination of small number statistics and the fact that the bottom right portion of the image has a slightly different magnification distribution according to our lens model. There also appears to be a detector artifact in the top left portion of each of the WFC3 pointings of ~ 250 arsec^2 that is likely impeding detection in those regions.

The properties of bright (m$_{H_{160},\rm int} < 25$) lower redshift objects that satisfy our z$_{850}$ (J$_{110}$) dropout color criteria but are rejected on account of S/N criteria, brightness cuts, or IR (*Spitzer*/Hawk-I) data are given in the top (bottom) of Table 2. Cutouts of these objects are also shown in the top (bottom) of Figure 4 and they are shown as red (magenta) circles in Figure 1. We also show the dust-reddened *Herschel* source HLS13 of Rex et al. (2010) as a white circle in Figure 1.

Low-mass stars (e.g., L and T Dwarfs), supernovae and active galactic nuclei are possible contaminants that will appear as point sources in our images. We take advantage of the high-resolution of WFC3/IR and the increased resolution due to lensing to determine which of our sources are resolved and which are not resolved and thus consistent with point sources. We do not attempt to estimate the sizes of those objects with m$_{H_{160}} > 26.5$ given the uncertainty in measuring low surface brightness objects. Only those objects with m$_{H_{160}} < 26.5$ are used below in the surface density and LF of Figures 7 and 9. All of these objects have measured FWHM greater than 0.26″ in J$_{110}$ and 0.21″ in H$_{160}$ which is above the PSF size (0.18″ in J$_{110}$ and 0.19″ in H$_{160}$). Thus contamination due to point sources is unimportant.

Object I of Table 2 has some characteristics consistent with being a counter-image of object 3 of Table 1. It satisfies the z$_{850}$ dropout color criteria. It has $J_{110} - H_{160}$ and $z_{850} - J_{110}$ colors consistent with object 3 within 1σ error bars. Both have shapes extended in the direction expected by the lens model for a $z > 6$ source, as can be seen in Figure 1 in which the critical curve (cyan line) of the lens model is overlaid and the positions of the two objects are shown. Finally, given the position of one of the images, the mass model predicts a counter-image in the vicinity of the other (we have also verified that according to the lens model, none of the other dropout

Table 2
A Partial Sample of z_{850} (top) and J_{110} (bottom) Dropout Contaminants

Contaminant	R.A.	Decl.	$m_{H_{160}} \pm \Delta_p$	$(J_{110} - H_{160})$	$(z_{850} - J_{110})$	$m_{i_{775}}$	$m_{V_{606}}$
z_{850} A	104.69737	-55.965012	21.93±0.16	0.72±0.15	1.34±0.17	>28.1	>28.7
B	104.60057	-55.957890	21.64±0.16	0.67±0.15	1.51±0.17	24.67±0.23	26.81±0.37
C	104.61086	-55.927860	23.53±0.16	0.62±0.15	1.62±0.38	25.24±0.25	24.81±0.24
D	104.60263	-55.957169	20.30±0.16	0.75±0.15	1.46±0.17	23.44±0.23	25.19±0.23
E	104.64615	-55.970993	22.62±0.16	0.86±0.15	1.47±0.17	25.37±0.25	27.21±1.07
F	104.69501	-55.975872	23.14±0.16	0.62±0.15	1.25±0.25	26.31±0.23	25.86±0.23
G	104.62870	-55.970612	21.96±0.16	0.62±0.15	1.38±0.17	24.64±0.23	25.58±0.23
H	104.69444	-55.972286	22.49±0.16	0.51±0.15	1.53±0.17	>28.1	>28.7
I[*]	104.64444	-55.965549	24.18±0.16	0.34±0.15	1.36±0.26	25.70±0.24	27.23±0.73
J_{110} J	104.64898	-55.971981	23.12±0.16	1.19±0.15	2.51±0.48	26.78±0.37	>28.7
K	104.69546	-55.969612	23.10±0.16	1.23±0.15	1.45±0.63	>28.1	>28.7
L	104.63338	-55.977394	23.69±0.16	1.62±0.15	2.05±1.08	28.16±1.58	>28.7

Note. — These objects have $m_{H_{160,int}} < 25$ (except object I) and satisfy our dropout color criteria but are rejected from our sample as low redshift galaxies on account of S/N selection criteria, brightness cuts, or IR (*Spitzer*/Hawk-I) data. Similar photometric errors are due to assigning the minimum error discussed in Section 4. Objects A, B, and F lie very near a field edge (see Figure 1) and thus their photometry may be unreliable. Lower limits are the 1σ limiting magnitudes quoted in Section 2.

[*]This object has $m_{H_{160,int}} = 26.49 \pm 0.19$. See end of Section 5.4.

candidates would have observable counter-images).

However, this object also has characteristics inconsistent with being a counter-image of object 3. Its intrinsic H_{160} magnitude of 26.49 ± 0.19 differs significantly from that of object 3. However, the error on the magnification of object 3 is likely underestimated given that it lies close ($< 1''$) to the critical curve where the magnification changes rapidly with position (magnification errors are expected to be correct on average but may be under or overestimated for individual objects). Also, it is detected at 4.5σ in i_{775} and thus does not satisfy the S/N criterion of Equation 6.

6. COMPLETENESS

The completeness was estimated as function of redshift and observed H_{160} mangitude ($m_{H_{160}}$) with simulations using the IRAF task artdata. For each H_{160} magnitude, $m_{H_{160}} = (24, 25, 26, 27)$, we generated 100 mock galaxies at 25 different equally spaced redshifts in the range $5.5 < z < 10$. The colors of each galaxy were determined from a template spectrum, where again we follow Madau (1995) to apply an intergalactic medium absorption correction to the colors given the redshift. These galaxies were then added with a spatially uniform distribution to the $J_{110} + H_{160}$ images as stars convolved with a Tiny Tim PSF scaled to have FWHM of $(0.16, 0.17, 0.17, 0.18, 0.19)$ arcsec in V_{606}, $i775$, z_{850}, J_{110}, and H_{160}, respectively. We then attempt to detect these galaxies following the same procedure as the actual dropouts, meaning the galaxies must both be detected as well as satisfy the dropout color and S/N selection criteria. For each $m_{H_{160}}$ and z, the probability of detecting a galaxy as a dropout $p(m_{H_{160}}, z)$, or completeness, is simply the ratio of the number of galaxies detected as dropouts to the number of dropout galaxies added to the images. This completeness was estimated with five SEDs from the isochrone synthesis code of Bruzual & Charlot (2003) with instantaneous bursts and the following age and metallicity (Z in units of $Z_\odot$) combinations: 5 Myr and Z=0.02, 25 Myr

and Z=0.02, 100 Myr and Z=0.02, 100 Myr and Z=0.05, 100 Myr and Z=0.008. For our final completeness we use the average of the completeness estimates from each SED.

The completeness function gives us an estimate of the redshift distribution of our dropout samples. Figure 5 shows $p(m_{H_{160}} = 26, z)$ for our z_{850} and J_{110} dropout samples. The completeness is also used to correct the surface density of dropouts for incompleteness. To do this at a specific magnitude, say $m_{H_{160}} = m_0$, we correct the surface density using $p(m_0)$, the probability with which we detect dropout galaxies that have the redshift distribution given by $p(m_0, z)$. We find $p(m_{H_{160}}) = 58\%$, 54%, 40%, and 4% for $m_{H_{160}} = 24, 25, 26$, and 27, respectively. Once again this is the average of the completeness using each of five SEDs. As an example of how this varies with SED, the completeness at 26th magnitude ranged from 37% to 45% depending on the SED. Finally, $p(m_{H_{160}}, z)$ is also used to correct the LF of dropouts as described in Section 7.

The ICL (occupying $\sim 20 - 25\%$ of the search area) and obscuration by cluster members (obscuring $\sim 25\%$ of the area in the regions of the search area not near the ICL) are the two main factors that lower our completeness levels. Nevertheless, it is still advantageous to use clusters (like the Bullet Cluster) in the search for high redshift galaxies given that their magnifications facilitate reaching the more numerous faint sources overcompensating for the loss of search area obscured by the ICL. The above completeness is an average estimate over the entire search area, including the ICL.

We have estimated the completeness as a function of lensed magnitude, $p(m_{H_{160}})$, above. However, the completeness as a function of intrinsic magnitude, $p(m_{H_{160,int}})$, is required to estimate the intrinsic surface density. This is the probability that a galaxy in the source plane with intrinsic magnitude $m_{H_{160,int}}$ will be detected and satisfy our dropout color and S/N crite-
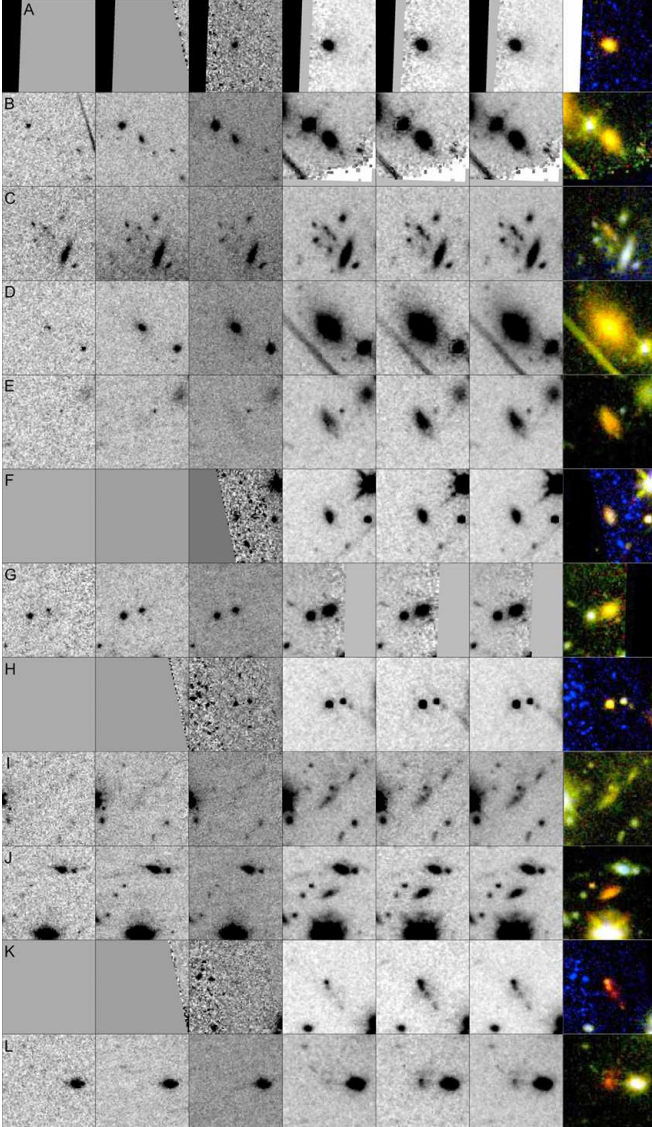
Figure 4. Cutouts of the partial sample of dropout contaminants of Table 2. These objects have $m_{H_{160,int}} < 25$ (except object I) and satisfy the z_{850} (top) and J_{110} (bottom) dropout color cuts but do not satisfy the other criteria. They are shown (from left to right) in V_{606}, i_{775}, z_{850}, J_{110}, H_{160}, $J_{110} + H_{160}$, and a $z_{850}J_{110}H_{160}$ color image. The labels correspond to the labels of Table 2. The cutouts are $7'' \times 7''$.

ria. It could be estimated by populating the source plane, properly lensing each object to the image plane, and estimating the completeness. This is difficult however given that the objects will be multiply-imaged. Therefore, we estimate $p\left(m_{H_{160,int}}\right)$ as the product of the probability $p\left(\mu\right)$ that a galaxy in the source plane will be magnified by μ and the probability $p\left(m_{H_{160}}\right)$ that if magnified by μ it will be detected as a dropout. This product is then summed over all possible magnifications from the lens model. This is given by

$$p\left(m_{H_{160,int}}\right) = \sum_{\mu} p\left(\mu\right) p\left(m_{H_{160}}\right), \qquad (10)$$

where $m_{H_{160}} = m_{H_{160,int}} - 2.5\log(\mu)$.

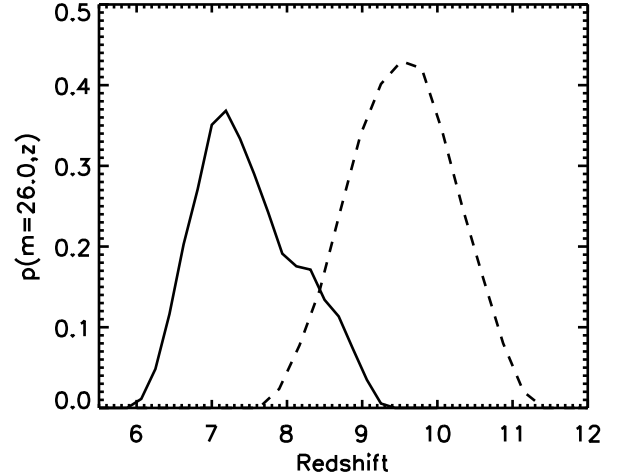We determine $p\left(\mu\right)$ (the distribution of μ values in the

Figure 5. For an LBG with $m_{H_{160}} = 26$, the probability of both detecting it and it satisfying our color and S/N criteria for z_{850} (*solid line*) and J_{110} (*dashed line*) dropouts is plotted as a function of redshift. The probability is averaged over 5 Bruzual & Charlot (2003) SEDs discussed in the text with varying ages and metallicities and then smoothed with a boxcar average over 5 points to better represent a more diverse set of spectra.

source plane) from the distribution of μ values in the image plane with each value weighted by the source plane area that it occupies (weighting $1/\mu$)[16]. This function is plotted in Figure 6 as a function of magnification in magnitudes. Following Equation 10 we find $p\left(m_{H_{160,int}}\right) = 56\%, 46\%, 21\%,$ and 5% for $m_{H_{160,int}} = 26, 27, 28,$ and 29, respectively. The completeness as a function of intrinsic magnitude and redshift, $p\left(m_{H_{160,int}}, z\right)$, used to correct the intrinsic LF below is also estimated following Equation 10 with $p\left(m_{H_{160}}\right)$ replaced by $p\left(m_{H_{160}}, z\right)$. We have performed a check by populating the source plane and ray-tracing objects with a simple lens model to confirm that the approach of Equation 10 is accurate.

7. SURFACE DENSITY AND LUMINOSITY FUNCTION

In this section we discuss our "lensed" (observed) and "intrinsic" (true, accounting for magnification) counts in terms of the surface density and LF. We also compare our counts with other surveys and discuss implications. Only those objects with lensed magnitudes $m_{H_{160}} < 26.5$ where the completeness is $> 22\%$ are considered here. This includes all objects in Table 1 except objects 1 and 2.

The completeness corrected surface density of our dropout sample is shown in Figure 7 for both lensed and intrinsic counts. We first discuss the lensed surface density. The lensed bins are 0.8 magnitudes wide and are centered at 25.4 and 26.2. The lensed or image plane area effectively observed as a result of the completeness is given by $A_{eff,len}\left(m_{H_{160}}\right) = p\left(m_{H_{160}}\right)\Omega_{img}$, where $\Omega_{img} = 8.27$ arcmin^2 is the image plane solid angle (outlined with the white dashed line in Figure 1). $A_{eff,len}\left(m_{H_{160}}\right)$ was applied to each bin by dividing each

---

[16] This does not account for multiple imaging of the source plane, which we find through simulations to be a small effect (see Section 7).
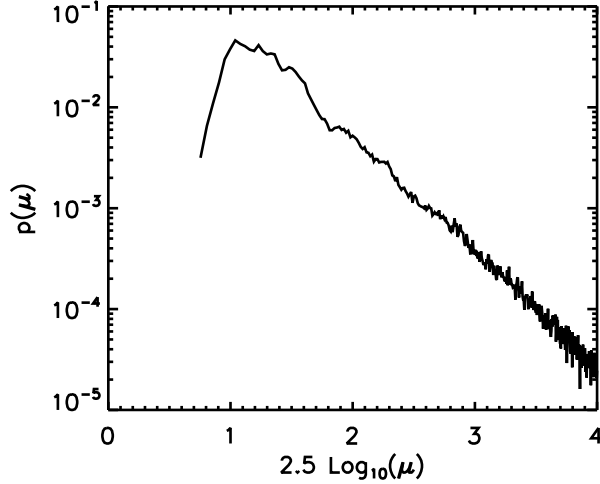
Figure 6. The probability, according to our lens model, that a galaxy placed randomly in the source plane will be magnified by $2.5 \log(\mu)$ magnitudes. The function is normalized such that $\sum_\mu p(\mu) = 1$.

dropout within the bin by $A_{\mathrm{eff,len}}(\mathrm{m}_{\mathrm{H}_{160}})$ linearly interpolated at the lensed magnitude of the dropout.
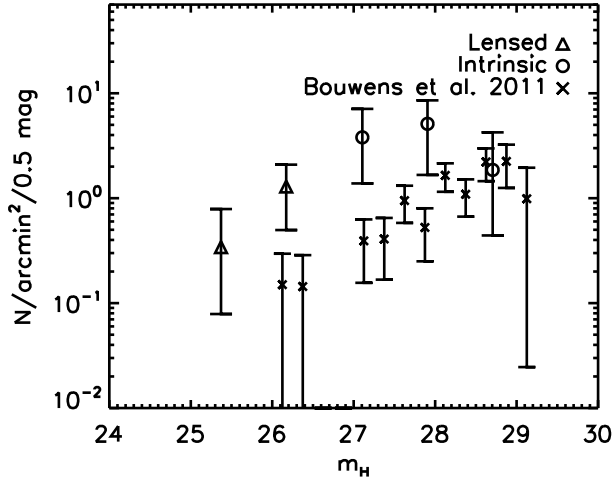

Figure 7. Lensed (*triangles*) and intrinsic (*circles*) completeness corrected surface density of z_{850} dropouts with bins of width 0.8 magnitudes. The lensed bins are centered at 25.4 and 26.2 and the intrinsic bins are centered at 27.1, 27.9, and 28.7. The counts are divided by the appropriate factor for comparison with data with 0.5 magnitude bins. The completeness corrected $z \sim 7$ counts of the HUDF09 blank field survey of Bouwens et al. (2011) are also shown for comparison (*X symbols*). We do not however expect our intrinsic counts to agree with those of Bouwens et al. (2011) given that we use different filters and thus have different redshift distributions. Uncertainty in our completeness estimate (see Section 6) is not reflected in the error bars.

For the intrinsic surface density, the bins are 0.8 magnitudes wide and are centered at 27.1, 27.9, and 28.7. The intrinsic apparent magnitude of each dropout was determined by dividing the flux by the magnification at the

source position. The cluster lens not only magnifies the brightness of the background galaxies but also magnifies the field of view, thus decreasing the observed solid angle. We estimate from the lens model a fractional decrease in solid angle of 0.19 ± 0.02. The uncertainty was estimated by evaluating the solid angle change using the map of magnification errors described in Section 3. While using the magnification maps for a different LBG redshift does change the positions of the critical curves (by $\sim 5''$ between $z = 5$ and $z \to \infty$, larger than the expected accuracy of the mass model), it changes the total solid angle of the field only negligibly (within the errors given above). The intrinsic or source plane area effectively observed as a result of the completeness (see e.g., Richard et al. 2008) is given by $A_{\mathrm{eff,int}}(\mathrm{m}_{\mathrm{H}_{160,\mathrm{int}}}) = p(\mathrm{m}_{\mathrm{H}_{160,\mathrm{int}}}) \Omega_{\mathrm{src}}$, where $\Omega_{\mathrm{src}} = 1.57$ arcmin^2 is the source plane solid angle. This function is shown in Figure 8. $A_{\mathrm{eff,int}}(\mathrm{m}_{\mathrm{H}_{160,\mathrm{int}}})$ was applied to each bin by dividing each dropout within the bin by $A_{\mathrm{eff,int}}(\mathrm{m}_{\mathrm{H}_{160,\mathrm{int}}})$ linearly interpolated at the intrinsic magnitude of the dropout. Our determination of the intrinsic surface density and LF does not account for some of the sources being multiply-imaged (i.e., a doubly imaged source is not counted twice). We have however verified with ray tracing, that in counting only the brightest source in the observational setup, the expected number counts change by only 15%, which is well within the error bars as discussed next.
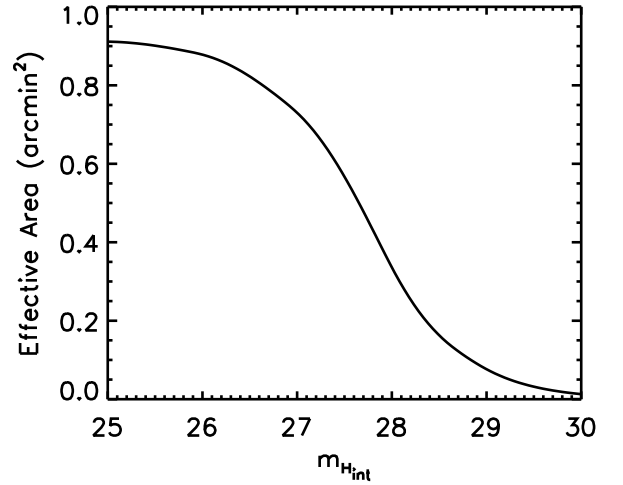

Figure 8. The source plane area effectively observed as a function of intrinsic H_{160} magnitude. This is the source plane area over which a galaxy with intrinsic magnitude $\mathrm{m}_{\mathrm{H}_{\mathrm{int}}}$ would be detected and satisfy our dropout selection criteria. The maximum possible area at a given intrinsic magnitude assuming 100% completeness is $\Omega_{\mathrm{src}} = 1.57$ arcmin^2.

Errors in the number of objects in our surface density and LF include both Poisson errors and sample variance due to large scale structure, added in quadrature. The Poisson errors[17] are the 95% confidence intervals from the Bayesian method of Kraft et al. (1991). We follow Somerville et al. (2004) in calculating the sam-

[17] We use the sum of the fraction of the 1σ error bars as the number of objects in each bin as discussed in Section 3.

ple variance and assume a power-law correlation function $\xi(r) = (r_0/r)^\gamma$. Given the lack of constraints on the clustering of LBGs at high redshifts, we assume that the clustering of Lyα emitters is sufficiently similar to inform our choice of γ and r_0 (see e.g., Nagamine et al. 2010). We fix $\gamma = 1.8$ and assume $r_0 = 7.0$ h^{-1}Mpc, which is conservative for $z \sim 7$ Lyα galaxies according to Orsi et al. (2008, Figure 5). This gives a relative sample standard deviation of $\sim 38\%$ for our 1.57 arcmin^2 intrinsic solid angle, in agreement with the sample variance calculator of Trenti & Stiavelli (2008) which gives 37%. Given our counts, Poisson errors dominate over sample variance.

The completeness corrected $z \sim 7$ counts of the HUDF09 blank field survey of Bouwens et al. (2011) are also shown in Figure 7. We expect our counts to be higher than those of Bouwens et al. (2011) as is the case. This is due to the fact that Bouwens et al. (2011) uses z_{850}, Y_{105} and J_{125} to search for z_{850} dropouts and given that Y_{105} and J_{125} combined cover the same wavelength range as our J_{110}, our redshift selection extends to higher redshift than that of Bouwens et al. (2011). We do obtain counts to only slightly shallower depths than the Bouwens et al. (2011) deep blank field survey with drastically less observation time, demonstrating the benefit of cluster surveys in the search for high redshift galaxies. In addition, by searching for galaxies behind the Bullet Cluster we see galaxies magnified by factors of 2-12 (0.75-2.7 magnitudes).

The completeness corrected LF of our dropout sample is shown in Figure 9 as a function of both lensed and intrinsic magnitudes. The best-fit $z \sim 7$ LF of Bouwens et al. (2011) is also shown. We first discuss the lensed LF. The bins are 0.8 magnitudes wide and centered at -21.5 and -20.7. The lensed LF was calculated following Steidel et al. (1999). The lensed comoving volume effectively observed as a result of the completeness is a function of lensed H_{160} magnitude given by

$$V_{\mathrm{eff,len}}\left(\mathrm{m}_{H_{160}}\right) = \Omega_{img} \int dz \frac{dV}{dz} p\left(\mathrm{m}_{H_{160}}, \mathrm{z}\right), \quad (11)$$

where $dz\,(dV/dz)$ is the comoving volume per unit solid angle between redshift z and $z+dz$ and $p\left(\mathrm{m}_{H_{160}}, \mathrm{z}\right)$ is the probability that an LBG of lensed magnitude $\mathrm{m}_{H_{160}}$ at redshift z will be detected in our images and satisfy our selection criteria (see Section 6). An estimate of the completeness corrected comoving number density of galaxies per magnitude bin (the LF) is then given by the lensed surface density (before dividing by $A_{\mathrm{eff,len}}$) divided by $V_{\mathrm{eff,len}}\left(\mathrm{m}_{H_{160}}\right)$ and the binsize. $V_{\mathrm{eff,len}}\left(\mathrm{m}_{H_{160}}\right)$ was applied to each bin by dividing each dropout within the bin by $V_{\mathrm{eff,len}}\left(\mathrm{m}_{H_{160}}\right)$ linearly interpolated at the lensed magnitude of the dropout. The error bars include sample variance and Poisson errors as described above. The fact that our lensed counts are significantly higher than the Bouwens et al. (2011) LF demonstrates the benefit of cluster surveys in this magnitude range as a result of the steepness of the LF leading to a positive magnification bias (see Section 1).

We now discuss the intrinsic LF. The bins are 0.8 magnitudes wide and centered at -19.8, -19, and -18.2. $V_{\mathrm{eff,int}}\left(\mathrm{m}_{H_{160,int}}\right)$ is the intrinsic comoving volume effectively observed as a result of the completeness. It
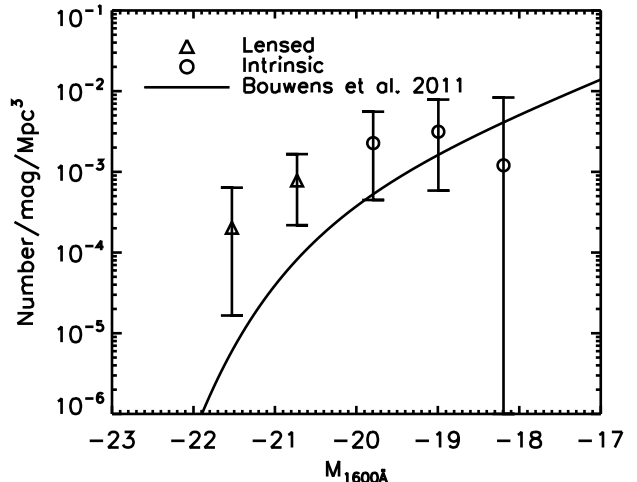

Figure 9. Lensed (*triangles*) and intrinsic (*circles*) luminosity function of z_{850} dropouts with bins of width 0.8 magnitudes. The lensed bins are centered at -21.5 and -20.7 and the intrinsic bins are centered at -19.8, -19, and -18.2. The Schechter parameterization of the best-fit luminosity function of the blank field study of Bouwens et al. (2011) is shown for comparison (*solid line*, $\phi^* = 0.9 \times 10^{-3}$ Mpc^{-3}, M$^* = -20.11$, and $\alpha = -1.94$). Uncertainty in our completeness estimate (see Section 6) is not reflected in the error bars.

is a function of intrinsic magnitude calculated following Equation 11 with Ω_{img} replaced by Ω_{src} and $p\left(\mathrm{m}_{H_{160}}, \mathrm{z}\right)$ replaced by $p\left(\mathrm{m}_{H_{160,int}}, \mathrm{z}\right)$. The intrinsic LF is then given by the intrinsic surface density (before dividing by $A_{\mathrm{eff,int}}$) divided by $V_{\mathrm{eff,int}}\left(\mathrm{m}_{H_{160,int}}\right)$ and the binsize. $V_{\mathrm{eff,int}}\left(\mathrm{m}_{H_{160,int}}\right)$ was applied to each bin by applying it to each dropout within the bin given its intrinsic magnitude.

Our intrinsic LF is in agreement with that of Bouwens et al. (2011). It is not our intent to constrain the LF given so few objects, but we do provide further proof of the concept that cluster searches for high redshift LBGs are not only feasible but in many ways preferable. These cluster surveys also provide an independent check of high redshift blank field results at much lower observing cost. With a larger sample of massive clusters, with well understood magnification and magnification error properties (at least 2 multiply-imaged systems with known redshifts and weak-lensing data) and observed to similar depths as the Bullet Cluster, we can increase the number counts and significantly reduce the errors due to sample variance and Poisson sampling.

8. CONCLUSIONS

We find 10 candidate $z \sim 7$ z_{850} dropout galaxies behind the Bullet Cluster. Using the 8 objects with $\mathrm{m}_{H_{160}} < 26.5$, where the completeness is greater than 22%, we calculate the surface density and luminosity function as a function of their intrinsic brightnesses. We find results consistent with published blank field surveys. We thus provide an independent check of blank field results at only slightly shallower depths. The magnifications of our z_{850} dropouts range from 2-12 allowing us to detect sources up to 2.7 magnitudes deeper than blank field surveys with the same exposure time. With the

magnification of the Bullet Cluster we are thus able to probe to similar depths as blank field surveys despite using much shallower data.

In searching for high redshift LBGs, we find 8 (3) objects with $m_{H_{160},int} < 25$ that although they do not satisfy some of our z_{850} (J_{110}) dropout selection criteria and are thus rejected as low redshift contaminants, they are sufficiently red to satisfy our color cuts and are thus interesting in their own right. We give their positions and photometric properties.

Magnifications are calculated from an optimally combined weak and strong lensing mass reconstruction of the Bullet Cluster (Bradač et al. 2009). Errors on the magnification are smaller than the Poisson sampling and sample variance. With more clusters with mass models of similar quality as the Bullet Cluster we could significantly reduce these errors and probe the luminosity function at greater depths and higher redshifts than is otherwise possible. With a larger sample of efficient lenses we would also expect to find many highly magnified images, which would allow for better morphological studies and greatly ease the spectroscopic follow up of $z \gtrsim 7$ galaxies.

REFERENCES

Altieri, B., et al. 1999, A&A, 343, L65
Bartelmann, M., & Schneider, P. 2001, Phys. Rep., 340, 291
Beckwith, S. V. W., et al. 2006, AJ, 132, 1729
Bertin, E., & Arnouts, S. 1996, A&AS, 117, 393
Blain, A. W., Kneib, J.-P., Ivison, R. J., & Smail, I. 1999, ApJ, 512, L87
Bouwens, R. J., Illingworth, G. D., Franx, M., & Ford, H. 2007, ApJ, 670, 928
—. 2008, ApJ, 686, 230
Bouwens, R. J., et al. 2009, ApJ, 690, 1764
—. 2011, ApJ, 737, 90
Bradač, M., et al. 2006, ApJ, 652, 937
—. 2009, ApJ, 706, 1201
Bradley, L. D., et al. 2008, ApJ, 678, 647
—. 2011, ArXiv:1104.2035
Broadhurst, T. J., Taylor, A. N., & Peacock, J. A. 1995, ApJ, 438, 49
Bruzual, G., & Charlot, S. 2003, MNRAS, 344, 1000
Castellano, M., et al. 2010a, A&A, 511, A20+
—. 2010b, A&A, 524, A28+
Chary, R., & Elbaz, D. 2001, ApJ, 556, 562
Clowe, D., et al. 2006, A&A, 451, 395
Coe, D., Benítez, N., Sánchez, S. F., Jee, M., Bouwens, R., & Ford, H. 2006, AJ, 132, 926
Coleman, G. D., Wu, C., & Weedman, D. W. 1980, ApJS, 43, 393
Diego, J. M., Tegmark, M., Protopapas, P., & Sandvik, H. B. 2007, MNRAS, 375, 958
Ellis, R., Santos, M. R., Kneib, J., & Kuijken, K. 2001, ApJ, 560, L119

Fan, X., et al. 2006, AJ, 132, 117
Fazio, G. G., et al. 2004, ApJS, 154, 10
Ford, H. C., et al. 2003, in Society of Photo-Optical Instrumentation Engineers (SPIE) Conference Series, Vol. 4854, Society of Photo-Optical Instrumentation Engineers (SPIE) Conference Series, ed. J. C. Blades & O. H. W. Siegmund, 81–94
Giavalisco, M. 2002, ARA&A, 40, 579
Giavalisco, M., et al. 2004, ApJ, 600, L103
Gonzalez, A. H., Clowe, D., Bradač, M., Zaritsky, D., Jones, C., & Markevitch, M. 2009, ApJ, 691, 525
Gonzalez, A. H., Papovich, C., Bradač, M., & Jones, C. 2010, ApJ, 720, 245
Henry, A. L., Malkan, M. A., Colbert, J. W., Siana, B., Teplitz, H. I., & McCarthy, P. 2008, ApJ, 680, L97
Hook, R., Stoehr, F., & Krist, J. 2008, Space Telescope European Coordinating Facility Newsletter, 44, 11
Jee, M. J., et al. 2007, ApJ, 661, 728
Kimble, R. A., MacKenty, J. W., O'Connell, R. W., & Townsend, J. A. 2008, in Society of Photo-Optical Instrumentation Engineers (SPIE) Conference Series, Vol. 7010, Society of Photo-Optical Instrumentation Engineers (SPIE) Conference Series
Kissler-Patig, M., et al. 2008, A&A, 491, 941
Knapp, G. R., et al. 2004, AJ, 127, 3553
Kneib, J., Ellis, R. S., Santos, M. R., & Richard, J. 2004, ApJ, 607, 697
Kneib, J., et al. 2003, ApJ, 598, 804
Koekemoer, A. M., Fruchter, A. S., Hook, R. N., & Hack, W. 2002, in The 2002 HST Calibration Workshop : Hubble after the Installation of the ACS and the NICMOS Cooling System, ed. S. Arribas, A. Koekemoer, & B. Whitmore, 337–+
Kraft, R. P., Burrows, D. N., & Nousek, J. A. 1991, ApJ, 374, 344
Labbé, I., et al. 2010, ApJ, 708, L26
Larson, D., et al. 2011, ApJS, 192, 16
Limousin, M., et al. 2007, ApJ, 668, 643
Madau, P. 1995, ApJ, 441, 18
Merten, J., Cacciato, M., Meneghetti, M., Mignone, C., & Bartelmann, M. 2009, A&A, 500, 681
Metcalfe, L., et al. 2003, A&A, 407, 791
Nagamine, K., Ouchi, M., Springel, V., & Hernquist, L. 2010, PASJ, 62, 1455
Natarajan, P., & Kneib, J.-P. 1996, MNRAS, 283, 1031
Oke, J. B., & Gunn, J. E. 1983, ApJ, 266, 713
Orsi, A., Lacey, C. G., Baugh, C. M., & Infante, L. 2008, MNRAS, 391, 1589
Rex, M., et al. 2010, A&A, 518, L13+
Richard, J., Pelló, R., Schaerer, D., Le Borgne, J., & Kneib, J. 2006, A&A, 456, 861
Richard, J., Stark, D. P., Ellis, R. S., George, M. R., Egami, E., Kneib, J.-P., & Smith, G. P. 2008, ApJ, 685, 705
Santos, M. R., Ellis, R. S., Kneib, J.-P., Richard, J., & Kuijken, K. 2004, ApJ, 606, 683
Schechter, P. 1976, ApJ, 203, 297
Schlegel, D. J., Finkbeiner, D. P., & Davis, M. 1998, ApJ, 500, 525
Sirianni, M., et al. 2005, PASP, 117, 1049
Smith, G. P., Kneib, J.-P., Smail, I., Mazzotta, P., Ebeling, H., & Czoske, O. 2005, MNRAS, 359, 417
Somerville, R. S., Lee, K., Ferguson, H. C., Gardner, J. P., Moustakas, L. A., & Giavalisco, M. 2004, ApJ, 600, L171
Soucail, G. 1990, Ap&SS, 170, 283
Stark, D. P., Ellis, R. S., Bunker, A., Bundy, K., Targett, T., Benson, A., & Lacy, M. 2009, ApJ, 697, 1493
Stark, D. P., Ellis, R. S., Richard, J., Kneib, J.-P., Smith, G. P., & Santos, M. R. 2007, ApJ, 663, 10
Steidel, C. C., Adelberger, K. L., Giavalisco, M., Dickinson, M., & Pettini, M. 1999, ApJ, 519, 1
Trenti, M., & Stiavelli, M. 2008, ApJ, 676, 767
Tucker, W. H., Tananbaum, H., & Remillard, R. A. 1995, ApJ, 444, 532
Vanzella, E., et al. 2009, ApJ, 695, 1163
—. 2011, ApJ, 730, L35+
Zheng, W., et al. 2009, ApJ, 697, 1907